# Matrix-Free Time-Domain Method for General Electromagnetic Analysis in 3-D Unstructured Meshes—Modified-Basis Formulation

Jin Yan, *Graduate Student Member, IEEE*, and Dan Jiao, *Fellow, IEEE*

*Abstract*—We develop a new matrix-free time-domain method, which requires no matrix solution, in unstructured meshes for general 3-D electromagnetic analysis. The method handles arbitrary unstructured meshes with the same ease as a finite-element method. Meanwhile, it is free of matrix solutions manifested by a naturally diagonal mass matrix, just like a finite-difference time-domain method. Different from our previous formulation where traditional curl-conforming vector bases are employed, modified vector bases are developed in this paper to directly connect the unknown coefficients of the vector basis functions employed to represent E (or H) with the unknowns obtained from the curl of H (or E), without any need for transformation. The proposed method employs only a single mesh. It does not require any interpolation and projection to obtain one field unknown from the other. Its accuracy and stability are guaranteed theoretically. Numerous experiments on unstructured triangular prism and tetrahedral meshes, involving both homogeneous and inhomogeneous and lossy materials, demonstrate the generality, accuracy, stability, and computational efficiency of the proposed method. The modified higher order vector bases developed in this paper can also be used in any other method that employs higher order bases to obtain an explicit relationship between unknown fields and unknown coefficients of vector bases.

*Index Terms*—Electromagnetic analysis, finite-difference time-domain (FDTD) method, higher order vector basis, matrix-free method, time-domain finite-element method (TDFEM), time-domain method, unstructured mesh.

## I. INTRODUCTION

AMONG time-domain methods for solving electromagnetic problems, the finite-difference time-domain (FDTD) method [1], [2] has its merits in being simple and free of a system matrix solution (matrix-free). However, it has been difficult to extend the FDTD to arbitrary unstructured meshes with theoretically guaranteed accuracy and stability. Dual mesh is, in general, required in nonorthogonal FDTD methods [3]–[15]. Such a dual mesh is not straightforward to construct for a primary mesh that must capture arbitrarily shaped material discontinuities in 3-D settings. In an arbitrary unstructured mesh, the dual mesh may not even exist. In addition, in the existing nonorthogonal FDTD schemes, both primary and dual field unknowns are placed along the edges of the mesh, and assumed to be constant. From such a discretization of field unknowns, the dual fields obtained from the primary ones are only second-order accurate at the center point of the primary-field loop, and along the direction perpendicular to the area of this loop. Elsewhere and/or along other directions, the dual fields do not have second-order accuracy. However, in a general unstructured mesh, the points and directions, where the dual field unknowns can be accurately obtained, are not coincident with the points and directions where the dual field unknowns are located. As a result, we observe that interpolation and projection are employed to obtain one field from the other field. However, the accuracy of the resultant scheme is not guaranteed in an irregular mesh. Meanwhile, the interpolation and projection techniques can also negatively affect the stability of the time marching, since they have changed the way the curl operators are discretized. In addition, the curl operator for **E**, in general, cannot be made reciprocal to that for **H** in an unstructured mesh. This results in an unsymmetrical curl–curl operator. Such an operator can support complex-valued and even negative eigenvalues. The resultant explicit time marching can be proved to be absolutely unstable [11], [16].

The time-domain finite-element method (TDFEM) [17] has great flexibility in dealing with any unstructured mesh, but it is not matrix-free, requiring the solution of a mass matrix. Mass lumping is known to be error prone. Orthogonal vector bases have been developed [18], [19]. However, an approximate integration rule is utilized to diagonalize the mass matrix. In the discontinuous Galerkin time-domain methods [20], [21], small local matrices are solved. However, this is because the field's tangential continuity is not enforced at the same time instant. Instead, the flux is communicated between adjacent elements. Building local matrices of small sizes is equivalent to moving the crosstalk terms in the original system matrix to the right-hand side of the system matrix equation, which can also be viewed as an iterative solution of the original matrix equation. The accuracy and convergence of such a solution in time domain are dependent on the problems being simulated and the time step used.

In this paper, we develop a new matrix-free time-domain method for arbitrary unstructured meshes. This method

The authors are with the School of Electrical and Computer Engineering, Purdue University, West Lafayette, IN 47907 USA (e-mail: yan107@purdue.edu; djiao@purdue.edu).

handles arbitrary unstructured meshes with the same ease as an FEM. Meanwhile, advantageous to the FEM, this new time-domain method produces a naturally diagonal mass matrix regardless of the element shape used for discretization. Hence, it facilitates a matrix-free solution of Maxwell's equations. Different from the existing nonorthogonal FDTD methods, the new method does not involve the use of dual mesh, interpolation, and projection. It employs only a single mesh. Furthermore, the electric field unknowns obtained from the discretized magnetic fields are exactly the same as the electric field unknowns used in the discretization of Faraday's law. Similarly, the magnetic field unknowns obtained from the discretized electric fields are exactly equal to the magnetic field unknowns used in the discretization of Ampere's law, without any need for interpolation and projection. Such an algorithm ensures the accuracy of the resulting discretization of Maxwell's equations. Moreover, the tangential continuity of the fields is enforced across element interfaces. In addition, the new method overcomes the absolute instability of an explicit method when simulating an unsymmetrical operator whose eigenvalues are complex and even negative. Such an operator is often unavoidable in an unstructured mesh. Higher order accuracy can also be flexibly achieved in the proposed method for both **E** and **H** fields.

In our NEMO conference paper [22], we present detailed 2-D formulations of a matrix-free time-domain method in unstructured meshes, which are not given in [23]. In [16] and [24], we provide a 3-D formulation based on traditional vector basis functions. In this paper, based on our preliminary work reported in conference papers [25], [26], we develop a new 3-D matrix-free formulation by constructing a set of new vector bases modified from the original bases. As a result, the electric field unknowns obtained from the discretization of Ampere's law are made the same as the unknown coefficients of the vector basis functions used to expand **E** in Faraday's law. Hence, the transformation used in [16] is avoided between the two sets of unknowns. The discretized Faraday's law is thereby directly connected to the discretized Ampere's law without any need for transformation. This saves the computational cost in generating the transformation matrix and its related computation. Numerous numerical experiments have been conducted on a variety of 3-D unstructured meshes, for both homogeneous and inhomogeneous as well as lossy problems. Comparisons with analytical solutions and the results obtained from the TDFEM as well as our previous matrix-free formulation [16] have validated the proposed new matrix-free method.

## II. PROPOSED METHOD

Considering a general 3-D problem meshed into arbitrarily shaped elements, which can even be a mix of different shapes of elements, we start from the differential form of Faraday's law and Ampere's law

$$\nabla \times \mathbf{E} = -\mu \frac{\partial \mathbf{H}}{\partial t} \tag{1}$$

$$\nabla \times \mathbf{H} = \epsilon \frac{\partial \mathbf{E}}{\partial t} + \sigma \mathbf{E} + \mathbf{J} \tag{2}$$
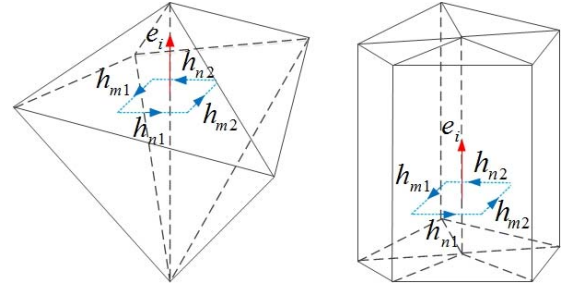


Fig. 1.   Illustration of magnetic field points and directions for obtaining $e_i$.

we pursue a discretization of the two equations in time domain, such that the resultant numerical system is free of matrix solutions.

### A. Discretization of Faraday's Law

In each element, we expand **E** by vector bases $\mathbf{N}_j$ ($j = 1, 2, \ldots, m$), obtaining

$$\mathbf{E} = \sum_{j=1}^{m} u_j \mathbf{N}_j \tag{3}$$

where $u_j$ is the $j$th basis's unknown coefficient. Substituting (3) into (1) to evaluate **H** at $\mathbf{r}_{hi}$ point and along the $\hat{h}_i$ direction, with $i = 1, 2, \ldots, N_h$, we have

$$\mathbf{S}_e \{u\} = -\text{diag}(\{\mu\}) \frac{\partial \{h\}}{\partial t} \tag{4}$$

where the $i$th entry of vector $\{h\}$ is

$$h_i = \mathbf{H}(\mathbf{r}_{hi}) \cdot \hat{h}_i \tag{5}$$

$\{u\}$ is of length $N_e$ consisting of all $u_j$ coefficients, $\text{diag}(\{\mu\})$ is a diagonal matrix of permeability, and $\mathbf{S}_e$ is a sparse matrix having the following entry:

$$\mathbf{S}_{e,ij} = \hat{h}_i \cdot \{\nabla \times \mathbf{N}_j\}(\mathbf{r}_{hi}). \tag{6}$$

Apparently, we have an infinite number of choices of **H** points and directions to build (4). However, to ensure the accuracy of the overall scheme which involves the discretization of not only Faraday's law but also Ampere's law, we should select the **H** points and directions in such a way that the resultant **H** fields can, in turn, generate desired **E** accurately. Although there are many choices to do so, the simplest choice is to choose a rectangular loop centering the **E** unknown and perpendicular to it, as shown in Fig. 1. Then, along this loop, we select the midpoint of each side as **H** point, and the unit vector tangential to each side as the **H**'s direction. The **H** fields obtained at these points and along these directions can certainly ensure the accuracy of **E** when we discretize Ampere's law. In addition, regardless of the element shape, there is no difficulty to define such a rectangular loop for each **E** unknown.

### B. Discretization of Ampere's Law

From Ampere's law, by evaluating **E** at $\mathbf{r}_{ei}$ point and along the $\hat{e}_i$ direction ($i = 1, 2, \ldots, N_e$), respectively, we obtain

$$\hat{e}_i \cdot \{\nabla \times \mathbf{H}\}(\mathbf{r}_{ei}) = \epsilon(\mathbf{r}_{ei}) \frac{\partial e_i}{\partial t} + \sigma(\mathbf{r}_{ei}) e_i + \hat{e}_i \cdot \mathbf{J}(\mathbf{r}_{ei}) \tag{7}$$

in which

$$e_i = \mathbf{E}(\mathbf{r}_{ei}) \cdot \hat{e}_i. \tag{8}$$

Based on the choice of $\mathbf{H}$ points and directions shown in Fig. 1, the $\hat{e}_i \cdot \nabla \times \mathbf{H}$ in (7) can be discretized accurately as

$$\hat{e}_i \cdot \{\nabla \times \mathbf{H}\}(\mathbf{r}_{ei}) = (h_{m1} + h_{m2})/l_{im} + (h_{n1} + h_{n2})/l_{in} \tag{9}$$

where $l_{im}$ is the distance between $h_{m1}$ and $h_{m2}$, while $l_{in}$ is the distance between $h_{n1}$ and $h_{n2}$, as shown in Fig. 1. With (9), (7) can be rewritten as

$$\mathbf{S}_h\{h\} = \mathrm{diag}\,(\{\epsilon\}) \frac{\partial \{e\}}{\partial t} + \mathrm{diag}\,(\{\sigma\})\,\{e\} + \{j\} \tag{10}$$

where $\{j\}$'s entries are $\hat{e}_i \cdot \mathbf{J}(\mathbf{r}_{ei})$, and $\mathrm{diag}(\{\epsilon\})$ and $\mathrm{diag}(\{\sigma\})$ are diagonal matrices whose entries are permittivity, and conductivity, respectively. Matrix $\mathbf{S}_h$ is the sparse of size $N_e \times N_h$, each row of which has four nonzero entries only being

$$\mathbf{S}_{h,ij} = 1/l_{ij} \tag{11}$$

where $j$ is the global index of the $\mathbf{H}$ unknown used to generate $e_i$, and $l_{ij}$ is simply the distance between the $\mathbf{E}$ point ($\mathbf{r}_{ei}$) and the $\mathbf{H}$ point ($\mathbf{r}_{hj}$) multiplied by two.

### C. Formulation of Modified Vector Basis Functions

Can we use zeroth-order vector basis functions in (3)? The answer is negative. This is because they produce a constant $\mathbf{H}$ field in each element. As a result, they fail to accurately generate the $\mathbf{H}$ fields at an arbitrary point along an arbitrary direction, and thereby at the points and along the directions desired for generating accurate $\mathbf{E}$. For example, the $\mathbf{H}$ fields desired at the points along the directions shown in Fig. 1 cannot be accurately obtained from zeroth-order vector basis functions. Hence, we propose to use higher order vector bases. However, they need modifications to satisfy

$$\{u\} = \{e\} \tag{12}$$

to connect (10) with (4) directly. As shown in (3), $\{u\}$ is the vector containing all the unknown coefficients of the vector basis functions; while $\{e\}$ is the vector of discretized electric fields, as shown in (8). They may not be the same. If we use the normalized zeroth-order vector bases, $\{u\} = \mathbf{E}(\mathbf{r}_{ei}) \cdot \hat{e}_i$, and therefore, (12) is satisfied. However, higher order curl-conforming bases [27] do not completely satisfy this property. In [16], we do not modify the original higher order vector bases. Instead, we find the relationship between $\{e\}$ and $\{u\}$, which is $\{e\} = \mathbf{P}\{u\}$, where $\mathbf{P}$ is a block diagonal matrix. We then use this relationship to connect (10) with (4). In this paper, we show by developing a set of modified higher order vector bases, we can make $\{u\}$ equal to $\{e\}$, and hence bypassing the need for transformation. This saves the computational cost of generating the transformation matrix $\mathbf{P}$ and its related computation.

To see the point why higher order curl-conforming bases do not satisfy (12) more clearly, we can substitute (3) into $e_i = \mathbf{E}(\mathbf{r}_{ei}) \cdot \hat{e}_i$, obtaining

$$e_i = \sum_{j=1}^{m} u_j \mathbf{N}_j(\mathbf{r}_{ei}) \cdot \hat{e}_i. \tag{13}$$
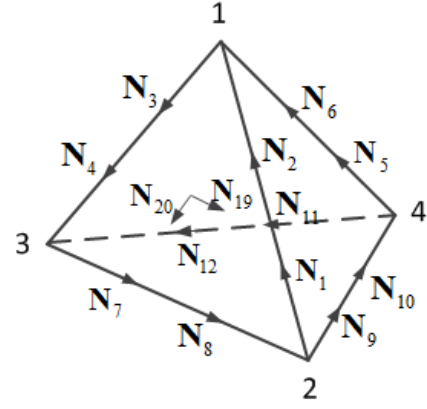


Fig. 2. Illustration of the first-order curl-conforming vector bases in a tetrahedral element.

Obviously, for (12) to hold true, it is required that

$$\mathbf{N}_j(\mathbf{r}_{ei}) \cdot \hat{e}_i = \delta_{ji}. \tag{14}$$

In other words, the $j$th vector basis's projection should be zero onto the direction and at the point associated with the $i$th vector basis's degree of freedom. This property is naturally satisfied by edge vector basis functions. To explain, along any edge, the unit vector associated with the vector basis defined on this edge is tangential to the edge. Hence, (14) is naturally satisfied, since it is how the curl-conforming vector bases ensure the tangential continuity of the fields at the element interface. However, in higher order vector bases, there also exist face vector basis functions and basis functions defined internal to the element. They, in general, do not satisfy the property of (14). Take the face vector bases as an example, their degrees of freedom are tangential to the face. However, each pair of the face vector bases is defined at the same point, and their directions are not perpendicular to each other. Hence, they do not satisfy the property of (14), and thus require modifications. Since first-order bases are sufficient for use in terms of generating second-order accuracy in the proposed method, next, we will use this set of bases as an example to show how to modify them. However, the essential idea applies to other higher order bases.

In a tetrahedral element, there are 20 first-order vector bases [27]. Among them, 12 bases are edge vector basis functions, as shown in Fig. 2. They are defined as

$$\begin{aligned} \mathbf{N}_1 &= (3\xi_2 - 1)\mathbf{W}_{21} & \mathbf{N}_2 &= (3\xi_1 - 1)\mathbf{W}_{21} \\ \mathbf{N}_3 &= (3\xi_1 - 1)\mathbf{W}_{13} & \mathbf{N}_4 &= (3\xi_3 - 1)\mathbf{W}_{13} \\ \mathbf{N}_5 &= (3\xi_4 - 1)\mathbf{W}_{41} & \mathbf{N}_6 &= (3\xi_1 - 1)\mathbf{W}_{41} \\ \mathbf{N}_7 &= (3\xi_3 - 1)\mathbf{W}_{32} & \mathbf{N}_8 &= (3\xi_2 - 1)\mathbf{W}_{32} \\ \mathbf{N}_9 &= (3\xi_2 - 1)\mathbf{W}_{24} & \mathbf{N}_{10} &= (3\xi_4 - 1)\mathbf{W}_{24} \\ \mathbf{N}_{11} &= (3\xi_4 - 1)\mathbf{W}_{43} & \mathbf{N}_{12} &= (3\xi_3 - 1)\mathbf{W}_{43} \end{aligned} \tag{15}$$

where $\xi_i (i = 1, 2, 3, 4)$ are the volume coordinates at four vertices, and $\mathbf{W}_{ij}$ denotes the zeroth-order basis associated with the edge connecting vertex $i$ to vertex $j$.

Basically, along each edge, there are two degrees of freedom of the vector bases, located at the points $\mathbf{r}_{ei}$ whose distance is

respectively 1/3, and 2/3 edge length to any one of the two nodes forming the edge. $\hat{e}_i$ associated with each edge basis is simply the unit tangential vector of the edge where the basis is defined. The 12 edge bases satisfy the property of (14).

However, the other eight vector bases defined on the four faces of the tetrahedron do not satisfy the property of (14). These eight face bases can be written as

$$\mathbf{N}_{13} = 4.5\xi_2\mathbf{W}_{43} \quad \mathbf{N}_{14} = 4.5\xi_3\mathbf{W}_{24}$$
$$\mathbf{N}_{15} = 4.5\xi_3\mathbf{W}_{41} \quad \mathbf{N}_{16} = 4.5\xi_4\mathbf{W}_{13}$$
$$\mathbf{N}_{17} = 4.5\xi_4\mathbf{W}_{21} \quad \mathbf{N}_{18} = 4.5\xi_1\mathbf{W}_{24}$$
$$\mathbf{N}_{19} = 4.5\xi_1\mathbf{W}_{32} \quad \mathbf{N}_{20} = 4.5\xi_2\mathbf{W}_{13}. \tag{16}$$

The locations $\mathbf{r}_{ei}(i = 13, 14, \ldots, 20)$ and corresponding unit vectors $\hat{e}_i$ associated with the eight face vector bases are

$$\hat{e}_{13} = \hat{t}_{43} \quad \mathbf{r}_{13} = (\xi_2 = \xi_3 = \xi_4 = 1/3, \xi_1 = 0)$$
$$\hat{e}_{14} = \hat{t}_{24} \quad \mathbf{r}_{14} = (\xi_2 = \xi_3 = \xi_4 = 1/3, \xi_1 = 0)$$
$$\hat{e}_{15} = \hat{t}_{41} \quad \mathbf{r}_{15} = (\xi_1 = \xi_3 = \xi_4 = 1/3, \xi_2 = 0)$$
$$\hat{e}_{16} = \hat{t}_{13} \quad \mathbf{r}_{16} = (\xi_1 = \xi_3 = \xi_4 = 1/3, \xi_2 = 0)$$
$$\hat{e}_{17} = \hat{t}_{21} \quad \mathbf{r}_{17} = (\xi_1 = \xi_2 = \xi_4 = 1/3, \xi_3 = 0)$$
$$\hat{e}_{18} = \hat{t}_{24} \quad \mathbf{r}_{18} = (\xi_1 = \xi_2 = \xi_4 = 1/3, \xi_3 = 0)$$
$$\hat{e}_{19} = \hat{t}_{32} \quad \mathbf{r}_{19} = (\xi_1 = \xi_2 = \xi_3 = 1/3, \xi_4 = 0)$$
$$\hat{e}_{20} = \hat{t}_{13} \quad \mathbf{r}_{20} = (\xi_1 = \xi_2 = \xi_3 = 1/3, \xi_4 = 0) \tag{17}$$

in which $\hat{t}_{ij}$ stands for a unit tangential vector along the edge connecting vertex $i$ to vertex $j$. As can be seen, at the center of each face, there are two vector bases defined. Obviously, they do not satisfy the property of (14). For example, $\mathbf{N}_{19}(\mathbf{r}_{20}) \cdot \hat{e}_{20}$ is not zero. This is because at the center point of the face formed by nodes 1–3, $\mathbf{N}_{19}$ is not perpendicular to $\hat{e}_{20}$ whose direction is along the edge connecting vertices 1–3.

If we rewrite (13) as

$$\{e\} = \mathbf{P}\{u\}. \tag{18}$$

$\mathbf{P}$ matrix obviously has the following entries:

$$\mathbf{P}_{ij} = \mathbf{N}_j(\mathbf{r}_{ei}) \cdot \hat{e}_i. \tag{19}$$

As shown in [16], with the first-order vector bases, $\mathbf{P}$ is block diagonal whose diagonal block dimension is either one or two. The diagonal block of size two corresponds to the two vector bases on each face, while each edge basis only corresponds to one diagonal entry, which is 1, in $\mathbf{P}$. Next, we show how to modify the face bases to make $\mathbf{P}$ an identity matrix.

Since the two face vector bases are defined at the same point, a linear combination of the two also makes a valid basis. The definitions of the face bases are hence not unique, which is also shown in [27]. We can modify them. To do so, we keep one face vector basis intact, but revise the other one. For a face having vertices $i$, $j$, and $k$, the two face bases we develop are

$$\mathbf{N}_{f_1} = 4.5\xi_i\mathbf{W}_{jk} \quad \hat{e}_{f_1} = \hat{t}_{jk} \tag{20}$$
$$\mathbf{N}_{f_2} = c\xi_j\xi_k\nabla\xi_i \quad \hat{e}_{f_2} = \frac{\hat{n}_f \times \mathbf{W}_{jk}}{||\hat{n}_f \times \mathbf{W}_{jk}||} \tag{21}$$

and for both face bases, their degrees of freedom are located at the face center, and hence,

$$\mathbf{r}_{f_1} = \mathbf{r}_{f_2} = (\xi_i = \xi_j = \xi_k = 1/3). \tag{22}$$

Clearly, $\mathbf{N}_{f_1}$ in (20) is kept the same as before. It is the second face basis $\mathbf{N}_{f_2}$ that is changed. In (20), $\xi_i$ denotes the volume coordinate associated with node $i$, $\mathbf{W}_{jk}$ is the normalized zeroth-order edge basis with the subscripts denoting the two nodes of an edge, unit vector $\hat{t}_{jk}$ points from node $j$ to $k$, $c$ is the normalization coefficient making $\mathbf{N}_{f_2} \cdot \hat{e}_{f_2} = 1$ at the face center, and unit vector $\hat{n}_f$ is normal to the face.

With the aforementioned modification, the revised first-order bases are equally complete, and meanwhile satisfying the desired property of (14). To see this point more clearly, now, we have

$$\mathbf{N}_{f_1}(\mathbf{r}_{f_2}) \cdot \hat{e}_{f_2} = 0$$
$$\mathbf{N}_{f_2}(\mathbf{r}_{f_1}) \cdot \hat{e}_{f_1} = 0. \tag{23}$$

The second row in the above holds true, because $\nabla\xi_i$ is perpendicular to $\hat{t}_{jk}$. As a result, the original nonzero off-diagonal terms in $\mathbf{P}$ become zero. In addition to satisfying (23), we also have to ensure that the modified second face basis does not bring any new change to the original $\mathbf{P}$, i.e., changing the original zeros in $\mathbf{P}$ to nonzeros. If this happens, then the new bases defined in (20) cannot achieve the goal of making (12) true. This can be examined by evaluating the entries residing in the column and the row in $\mathbf{P}$ corresponding to the second new face basis, as other rows and columns are not affected. Essentially, we have to assess the following entries to see whether they are zero:

$$\mathbf{P}_{f_2,i} = \mathbf{N}_{f_2}(\mathbf{r}_{ei}) \cdot \hat{e}_i \quad (i \neq f_2)$$
$$\mathbf{P}_{i,f_2} = \mathbf{N}_i(\mathbf{r}_{f_2}) \cdot \hat{e}_{f_2} \quad (i \neq f_2). \tag{24}$$

The entries of $\mathbf{P}_{f_2,i} = \mathbf{N}_{f_2}(\mathbf{r}_{ei}) \cdot \hat{e}_i$ reside on the row corresponding to the second face basis in $\mathbf{P}$. When $\mathbf{r}_{ei}$ and $\hat{e}_i$ correspond to an edge basis, $\mathbf{N}_{f_2} = 0$ since $\xi_j\xi_k = 0$ on all edges except for the edge connecting $j$ to $k$. On this edge, $\mathbf{N}_{f_2}$ is perpendicular to the edge, and hence, $\mathbf{N}_{f_2}(\mathbf{r}_{ei}) \cdot \hat{e}_i$ also vanishes. When $\mathbf{r}_{ei}$ and $\hat{e}_i$ belong to a face basis, $\mathbf{N}_{f_2} = 0$ since $\xi_j\xi_k = 0$ on all faces except for the two faces sharing edge connecting $j$ to $k$. On the same face where $\mathbf{N}_{f_2}$ is defined, as shown in (23), the corresponding $\mathbf{P}$ term is zero. On the other face, $\mathbf{N}_{f_2}$ is not zero; however, $\mathbf{N}_{f_2}$ is perpendicular to this face since it is along the direction of $\nabla\xi_i$. As a result, $\mathbf{N}_{f_2}(\mathbf{r}_{ei}) \cdot \hat{e}_i$ also vanishes. In summary, the modified new face basis preserves the original zeros in the row of this basis in $\mathbf{P}$, while vanishing the original nonzero entry in this row.

As for the entries of $\mathbf{P}_{i,f_2} = \mathbf{N}_i(\mathbf{r}_{f_2}) \cdot \hat{e}_{f_2}$, they are located in the column corresponding to the second face basis in $\mathbf{P}$. If basis $i$ is an edge basis, it is zero at the center points of three of the four faces and perpendicular to the fourth face. Hence, $\mathbf{P}_{i,f_2} = 0$. If basis $i$ is a face basis, it can be either the first face basis or the second face basis. If it is the first face basis, based on its expression shown in (20), among the other three faces where it is not located, it is zero on one of the three faces, and perpendicular to the rest two. Hence, $\mathbf{P}_{i,f_2} = 0$ if $i$-basis does not belong to the face where $f_2$-basis is defined. If $i$-basis and $f_2$-basis belong to the same face, from (23), $\mathbf{P}_{i,f_2}$ is also zero. If the basis $i$ is the second face basis, among the other three faces where it is not located, it is zero on two of the three faces, and perpendicular to the

rest one. Hence, $\mathbf{P}_{i, f_2}$ is also zero. As a result, the new change of the second face basis also preserves the original zeros in the column corresponding to the second face basis in $\mathbf{P}$, while vanishing the original nonzero entry in this column.

Based on (20), the complete set of modified face bases and their projection directions, in accordance with the notations of (16), can be written as follows:

$$
\begin{aligned}
\mathbf{N}_{14} &= c_{14}\xi_3\xi_4\nabla\xi_2 \quad \hat{e}_{14} = \frac{(\hat{n}_{234} \times \mathbf{W}_{43})}{||\hat{n}_{234} \times \mathbf{W}_{43}||} \\
\mathbf{N}_{16} &= c_{16}\xi_1\xi_4\nabla\xi_3 \quad \hat{e}_{16} = \frac{(\hat{n}_{134} \times \mathbf{W}_{41})}{||\hat{n}_{134} \times \mathbf{W}_{41}||} \\
\mathbf{N}_{18} &= c_{18}\xi_1\xi_2\nabla\xi_4 \quad \hat{e}_{18} = \frac{(\hat{n}_{124} \times \mathbf{W}_{21})}{||\hat{n}_{124} \times \mathbf{W}_{21}||} \\
\mathbf{N}_{20} &= c_{20}\xi_2\xi_3\nabla\xi_1 \quad \hat{e}_{20} = \frac{(\hat{n}_{123} \times \mathbf{W}_{32})}{||\hat{n}_{123} \times \mathbf{W}_{32}||}
\end{aligned} \quad (25)
$$

where $\hat{n}_{ijk}$ denotes a unit vector normal to the face formed by vertices $i$, $j$, and $k$.

The basic idea of the aforementioned approach to make $\hat{e}_i \cdot \mathbf{N}_j(\mathbf{r}_{ei}) = \delta_{ij}$ satisfied is to choose appropriate basis and projection directions of the second basis, when encountering a pair of bases defined at the same point. The projection direction of the second basis is chosen perpendicular to the first basis at the point where the second basis's degree of the freedom is located. Meanwhile, the basis direction of the second basis is chosen to be perpendicular to the projection direction of the first basis. The essential idea of this approach is equally applicable to higher order bases in other types of elements such as the triangular prism elements.

In a triangular prism element, there are 36 first-order bases. Among them, the three pairs of bases associated with the center of the upper face, the prism center, and the center of the lower face do not satisfy (14), while other bases satisfy. Similar to the treatment in a tetrahedron element, for the three sets, we keep the first basis, but modify the second basis. For the top face formed by nodes 1–3, we construct the following two bases and their projection directions:

$$
\mathbf{N}_{f_1} = 4.5\xi_1\zeta_1(2\zeta_1 - 1)\mathbf{W}_{23} \quad \hat{e}_{f_1} = \hat{t}_{23} \quad (26)
$$

$$
\mathbf{N}_{f_2} = c\xi_2\xi_3\zeta_1(2\zeta_1 - 1)\nabla\xi_1 \quad \hat{e}_{f_2} = \frac{(\hat{n}_f \times \mathbf{W}_{23})}{||\hat{n}_f \times \mathbf{W}_{23}||} \quad (27)
$$

where $\zeta_1 = 1$ on the upper face and 0 on the lower one, and $\mathbf{W}_{12}$ is the normalized zeroth-order vector basis defined on the edge connecting nodes 1and 2.

With the modified vector bases, the entries in sparse matrix $\mathbf{S}_e$ shown in (6) can be determined. Since each vector basis $\mathbf{N}_j$ has an analytical expression, $\nabla \times \mathbf{N}_j$ and thereby $\mathbf{S}_e$ can be analytically evaluated. In addition, when building $\mathbf{S}_e$, the field tangential continuity is rigorously enforced across the element interface, since $\{u\}$, which is also $\{e\}$ now with the newly developed modified bases, is shared in common by adjacent elements. This is the same as how an FEM ensures the tangential continuity of the electric field.

### D. Matrix-Free Time Marching

With $\{u\} = \{e\}$, we can solve (4) and (10) in a leapfrog way, which requires no matrix solutions. The two can also be combined to solve as the following:

$$
\frac{\partial^2\{e\}}{\partial t^2} + \text{diag}\left(\left\{\frac{\sigma}{\epsilon}\right\}\right)\frac{\partial\{e\}}{\partial t} + \mathbf{S}\{e\} = -\text{diag}\left(\left\{\frac{1}{\epsilon}\right\}\right)\frac{\partial\{j\}}{\partial t} \quad (28)
$$

where

$$
\mathbf{S} = \text{diag}\left(\left\{\frac{1}{\epsilon}\right\}\right)\mathbf{S}_h\text{diag}\left(\left\{\frac{1}{\mu}\right\}\right)\mathbf{S}_e. \quad (29)
$$

Obviously, the matrices in front of the second- and first-order time derivatives are both diagonal. Hence, the proposed method possesses a naturally diagonal mass matrix. Therefore, an explicit marching of (28), such as a central-difference-based time marching, is free of matrix solutions. However, a brute-force explicit marching of (28) is absolutely unstable, because $\mathbf{S}$ is not symmetric in an unstructured mesh and it can support complex-valued and even negative eigenvalues. This has been proved in [16].

The stability problem can be solved as follows. Basically, we can begin with the following backward-difference-based time marching of (28):

$$
\begin{aligned}
\{e\}^{n+1} - 2\{e\}^n + \{e\}^{n-1} + \Delta t\,\text{diag} \\
\times \left(\left\{\frac{\sigma}{\epsilon}\right\}\right)(\{e\}^{n+1} - \{e\}^n) + \Delta t^2\mathbf{S}\{e\}^{n+1} \\
= -\Delta t^2\text{diag}\left(\left\{\frac{1}{\epsilon}\right\}\right)\left(\frac{\partial\{j\}}{\partial t}\right)^{n+1}.
\end{aligned} \quad (30)
$$

Rearranging the terms in (30), we obtain

$$
\begin{aligned}
(\mathbf{D} + \Delta t^2\mathbf{S})\{e\}^{n+1} \\
= 2\{e\}^n - \{e\}^{n-1} + \Delta t\,\text{diag} \\
\times \left(\left\{\frac{\sigma}{\epsilon}\right\}\right)\{e\}^n - \Delta t^2\text{diag}\left(\left\{\frac{1}{\epsilon}\right\}\right)\left(\frac{\partial\{j\}}{\partial t}\right)^{n+1}
\end{aligned} \quad (31)
$$

where

$$
\mathbf{D} = \mathbf{I} + \Delta t\,\text{diag}\left(\left\{\frac{\sigma}{\epsilon}\right\}\right) \quad (32)
$$

which is diagonal. Front multiplying both sides of (31) by $\mathbf{D}^{-1}$, we obtain

$$
(\mathbf{I} + \tilde{\mathbf{M}})\{e\}^{n+1} = \mathbf{D}^{-1}\{f\} \quad (33)
$$

where

$$
\tilde{\mathbf{M}} = \Delta t^2\mathbf{D}^{-1}\mathbf{S} \quad (34)
$$

and $\{f\}$ is the right-hand side of (31).

Although the backward-difference-based (31) is stable for an infinitely large time step as analyzed in [16], we choose a time step based on the stability criterion of traditional explicit time marching. This time step satisfies

$$
\Delta t < \frac{1}{\sqrt{\rho(\mathbf{S})}}. \quad (35)
$$

It is also the time step required by accuracy when there is no fine feature relative to working wavelength, since the maximum eigenvalue's square root, $(|\lambda_{\max}|)^{1/2}$, corresponds to the maximum angular frequency present in the system response. With such a choice of time step, the spectral radius
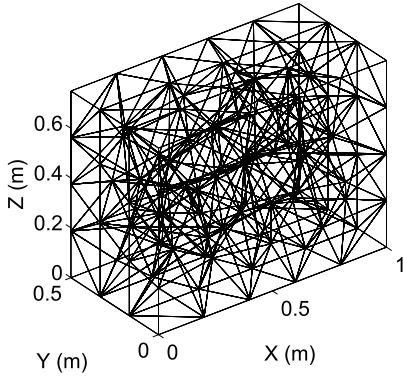
Fig. 3.   Illustration of the tetrahedron mesh of a $1 \times 0.5 \times 0.75$ m$^3$ rectangular box.

of $\tilde{\mathbf{M}}$ is guaranteed to be less than 1. This is because in this case, time step satisfies (35), and hence,

$$\Delta t^2 \rho(\mathbf{S}) < 1 \qquad (36)$$

in which $\rho(\cdot)$ denotes the spectral radius, which is the modulus of the largest eigenvalue. $\mathbf{D}$ is a diagonal matrix shown in (32). Hence,

$$\rho(\mathbf{D}^{-1}) = \frac{1}{\min_{1 \leq i \leq N_e}(1 + \Delta t \sigma_i / \epsilon_i)} = 1. \qquad (37)$$

We therefore obtain from (36) and (37)

$$\rho(\tilde{\mathbf{M}}) = \Delta t^2 \rho(\mathbf{D}^{-1}\mathbf{S}) \leq \Delta t^2 \rho(\mathbf{D}^{-1})\rho(\mathbf{S}) < 1. \qquad (38)$$

As a result, without loss of accuracy, the inverse of $\mathbf{I} + \tilde{\mathbf{M}}$ can be evaluated by

$$(\mathbf{I} + \tilde{\mathbf{M}})^{-1} = \mathbf{I} - \tilde{\mathbf{M}} + \tilde{\mathbf{M}}^2 - \tilde{\mathbf{M}}^3 + \cdots + (-\tilde{\mathbf{M}})^k \qquad (39)$$

where $k$ is guaranteed to be small since (38) is satisfied. Thus, the system matrix has an explicit inverse, and hence, no matrix solutions are required. Equation (33) can then be computed as

$$\{e\}^{n+1} = (\mathbf{I} - \tilde{\mathbf{M}} + \tilde{\mathbf{M}}^2 - \cdots + (-\tilde{\mathbf{M}})^k)\mathbf{D}_i\{f\} \qquad (40)$$

where $\mathbf{D}_i$ is the diagonal matrix $\mathbf{D}$'s inverse. The computational cost of (40) is $k$ sparse matrix-vector multiplications, since each term can be computed from the previous term recursively, thus efficient.

## III. Numerical Results

To validate the proposed new formulation-based matrix-free method, in this section, we simulate a variety of 3-D unstructured meshes. The aspect ratio of the mesh is defined as the longest edge length divided by the shortest edge length. The number of expansion terms $k$ used in (39) is nine for all examples simulated. The time step chosen is the same as that of the explicit TDFEM.

### A. Wave Propagation in a Tetrahedral Mesh of a 3-D Box

The first example is a 3-D free-space box of dimension $1 \times 0.5 \times 0.75$ m$^3$ discretized into tetrahedral elements. Its mesh is shown in Fig. 3 with 350 tetrahedral elements and 544 edges. The aspect ratio of the tetrahedral mesh is 3.67. To assess the accuracy of the proposed method, we simulate a free-space wave propagation problem, since its analytical solution is known.
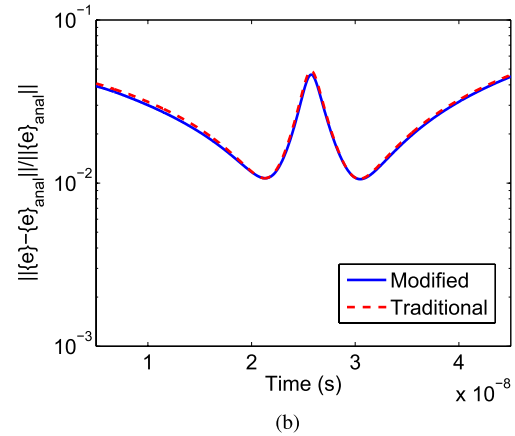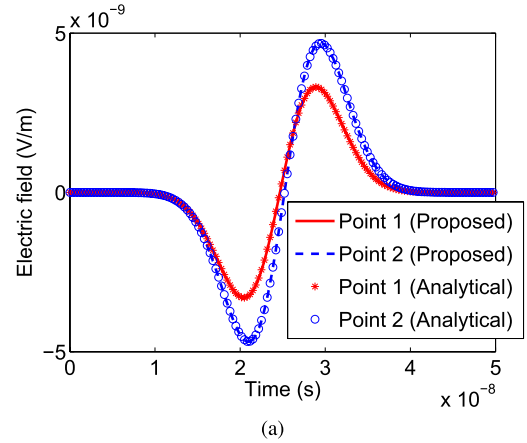


(a)



(b)

Fig. 4.   Simulation of a 3-D rectangular box discretized into tetrahedral elements. (a) Electric fields obtained from the proposed method as compared with analytical results. (b) Entire solution error as a function of time.

The incident $\mathbf{E}$, which is also the total field in the given problem, is specified as $\mathbf{E} = \hat{y}f(t - x/c_0)$, where $f(t) = 2(t - t_0)\exp(-(t - t_0)^2/\tau^2)$, $\tau = 6 \times 10^{-9}$ s, $t_0 = 4\tau$, and $c_0$ is the speed of light. The time step is chosen as $\Delta t = 1.6 \times 10^{-11}$ s. The proposed method takes only 2.12 MB to store sparse matrices $\mathbf{S}_e$ and $\mathbf{S}_h$, and $5.2 \times 10^{-4}$ s to finish the simulation at one time step. In Fig. 4(a), we plot the 1st and 1832th entries randomly selected from the unknown $\{e\}$ vector, which represent $\mathbf{E}(\mathbf{r}_{ei}) \cdot \hat{e}_i$ with $i = 1$ and 1832, respectively. It can be seen clearly that the results of the proposed method agree very well with the analytical solutions.

To examine the accuracy of all unknowns solved from the proposed method, and also across all time instants, we consider the relative error of the whole solution vector defined by

$$\text{Error}_{\text{entire}}(t) = \frac{||\{e\}_{\text{this}}(t) - \{e\}_{\text{ref}}(t)||}{||\{e\}_{\text{ref}}(t)||} \qquad (41)$$

as a function of time, where $\{e\}_{\text{this}}(t)$ denotes the entire unknown vector $\{e\}$ of length $N_e$ obtained from this method, whereas $\{e\}_{\text{ref}}(t)$ denotes the reference solution, which is analytical result $\{e\}_{\text{anal}}(t)$ in this example. In Fig. 4(b), we plot $\text{Error}_{\text{entire}}(t)$ across the whole time window in which the fields are not zero. It is evident that less than 4% error is observed at each time instant, demonstrating the accuracy of the proposed method. The center peak in Fig. 4(b) is due to the comparison with close to zero fields.
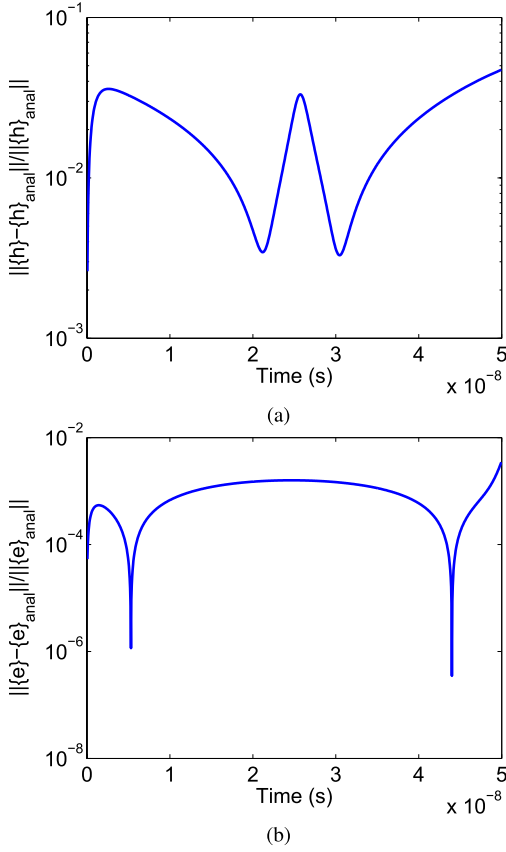
Fig. 5. (a) Entire solution error versus time of all $\mathbf{H}$ unknowns obtained from $\mathbf{S}_e$ rows of equations. (b) Entire solution error versus time of all $\mathbf{E}$ unknowns obtained from $\mathbf{S}_h$ rows of equations.
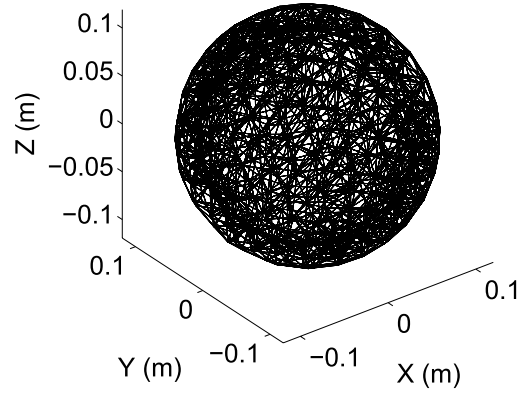


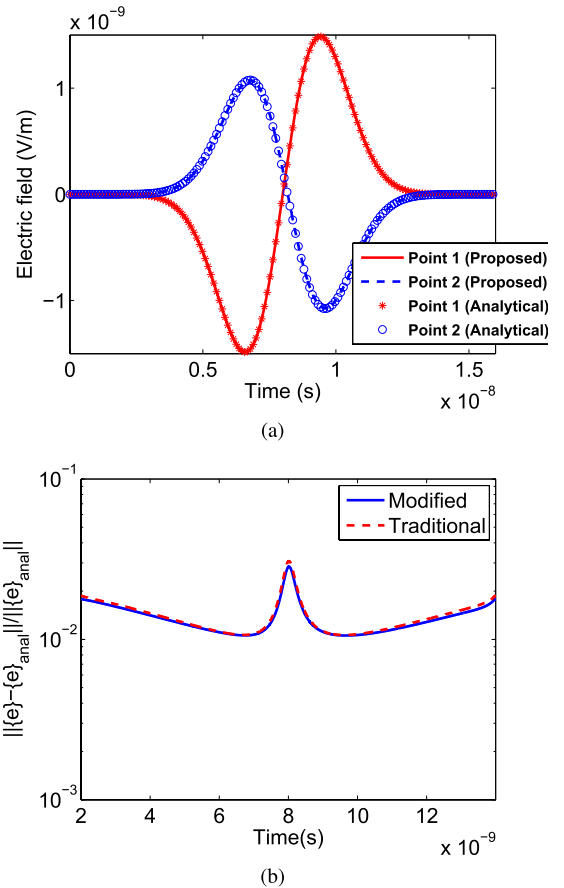Fig. 6. Illustration of the tetrahedron mesh of a solid sphere.



Fig. 7. Simulation of a sphere discretized into tetrahedral elements. (a) Electric fields obtained from the proposed method as compared with the analytical results. (b) Entire solution error as a function of time for $\mathbf{E}$.

This example has also been simulated in [16]. In Fig. 4(b), we compare the accuracy of the proposed new formulation with the formulation given in [16]. Obviously, the proposed new formulation with modified vector bases exhibits the same accuracy as the formulation given in [16].

In addition to the accuracy of the entire method, we have also examined the accuracy of $\mathbf{S}_e$, and $\mathbf{S}_h$ individually, since each is important to ensure the accuracy of the whole scheme. First, to solely assess the accuracy of $\mathbf{S}_e$, we perform the time marching of (4) only without (10) by providing an analytical $\{e\}$ to (4) at each time step. The resultant $\{h\}$ is then compared with analytical $\{h\}_{\text{anal}}$ at each time step. As can be seen from Fig. 5(a), where the following entire $\mathbf{H}$ solution error:

$$\frac{||h(t) - h_{\text{anal}}(t)||}{||h_{\text{anal}}(t)||} \tag{42}$$

is plotted with respect to time, the error of all $\mathbf{H}$ unknowns is $<3\%$ across the whole time window, verifying the accuracy of $\mathbf{S}_e$. Similarly, in order to examine the accuracy of $\mathbf{S}_h$, we perform the time marching of (10) only without (4) by providing an analytical $\{h\}$ to (10) at each time step. In Fig. 5(b), we plot (41) versus time. Again, very good accuracy is observed across the whole time window, verifying the accuracy of $\mathbf{S}_h$.

### B. Wave Propagation in a Tetrahedral Mesh of a Sphere

The second example is a sphere of radius 0.24 m centering at the origin. It is discretized into tetrahedral elements in free space, whose 3-D mesh is shown in Fig. 6. The mesh consists of 1987 tetrahedrons and 3183 edges. The aspect ratio of the tetrahedral mesh is 6.19. The outermost boundary is truncated by analytically known electric fields. The time step is $\Delta t = 2 \times 10^{-12}$ s. The same incident $\mathbf{E}$ is as that in the first example is used, but $\tau = 2 \times 10^{-9}$ s is chosen in accordance with the new structure's dimension.
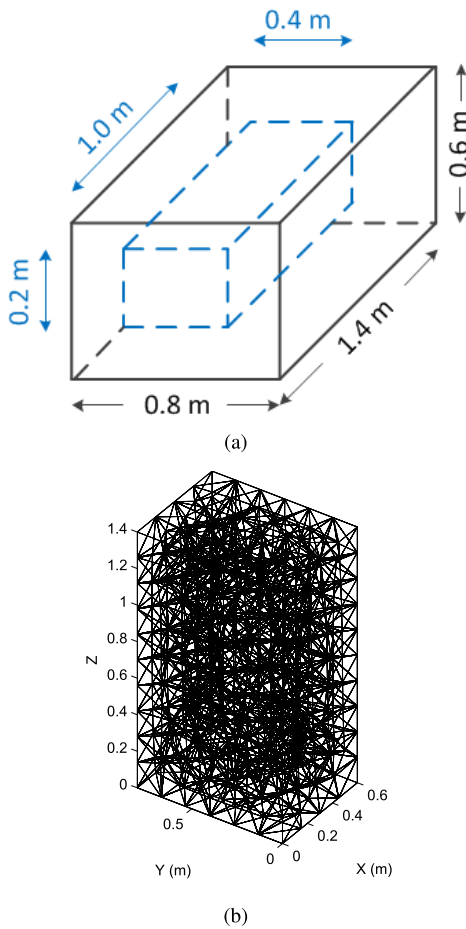
Fig. 8.　Illustration of a rectangular box with a hole. (a) Geometry. (b) Mesh details.
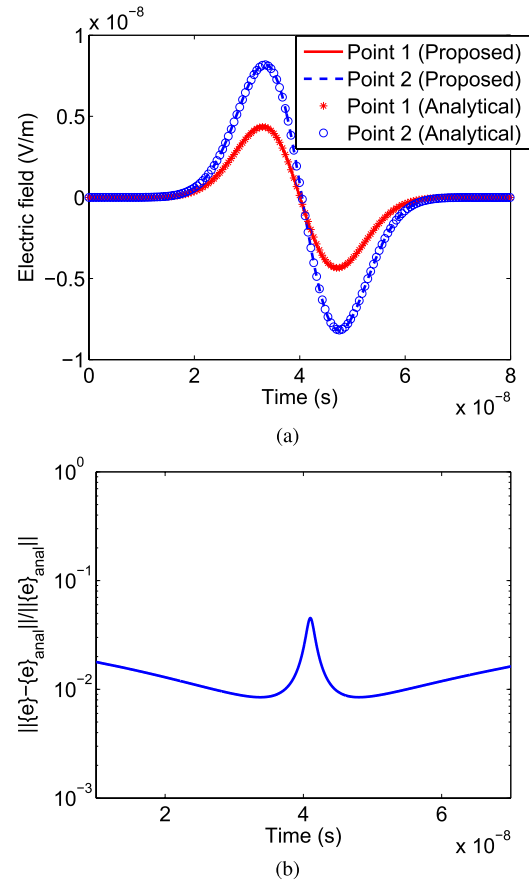


Fig. 9.　Simulation of a rectangular box with a hole discretized into tetrahedral elements. (a) Electric fields from the proposed method and those from analytical results. (b) Entire solution error versus time for **E**.

The proposed method takes only 10.07 MB to store sparse matrices $\mathbf{S}_e$ and $\mathbf{S}_h$, and 0.003 s to finish the simulation at one time step. Two randomly selected electric field unknowns, whose indices are 1 and 9762 in $\{e\}$, are shown in Fig. 7(a) against analytical data. Excellent agreement can be seen.

In Fig. 7(b), the entire solution error shown in (41) is plotted as a function of time, which is shown to be less than 3%. To compare the accuracy of the proposed new formulation having modified vector bases with that of the traditional vector bases in [16], the entire solution error obtained by the formulation in [16] is also shown in Fig. 7(b). Obviously, the two exhibit the same accuracy, validating the proposed new vector bases, and its resulting matrix-free formulation.

### C. Wave Propagation in a Tetrahedral Mesh of a Rectangular Box With a Hole

The third example is a rectangular box whose size is $0.6 \times 0.8 \times 1.4$ m$^3$ with a hole in the center, whose structure is shown in Fig. 8(a). Its mesh is shown in Fig. 8(b). The shape of the hole is also a rectangular box but of size $0.2 \times 0.4 \times 1$ m$^3$. It is discretized into tetrahedral elements having 1637 tetrahedrons and 2456 edges. The aspect ratio of the tetrahedral mesh is 5.36. The time step is chosen as $\Delta t = 2 \times 10^{-11}$ s. A free-space wave propagation problem is simulated in the given mesh, with the same incident **E** the

same as that of the first example, except for $\tau = 1 \times 10^{-8}$ s. Both the innermost and outermost boundaries of the mesh are truncated by analytically known electric fields.

The proposed method takes 9.89 MB to store sparse matrices $\mathbf{S}_e$ and $\mathbf{S}_h$, and $2.7 \times 10^{-3}$ s to finish the simulation at one time step. We randomly select the 1st and 8612th entries of vector $\{e\}$, and plot them in Fig. 9(a) in comparison with analytical solution. Excellent agreement can be observed. To assess the error of the entire $\{e\}$, we plot the entire solution error in Fig. 9(b) with respect to time, which again reveals good accuracy. In this example, we have also simulated to very late time to examine late-time stability. As can be seen from Fig. 10, the proposed method is stable.

### D. Wave Propagation in a Spherical Shell

This example is a spherical shell whose inner radius is 0.8 m, and outer radius is 1.2 m. It is discretized into tetrahedral elements in free space. The discretization results in 2704 edges and 1956 tetrahedrons. The aspect ratio of the tetrahedral mesh is 5.67. The incident **E** is the same as that of the first example, except for $\tau = 4 \times 10^{-8}$ s.

Analytically known electric fields are imposed to truncate the computational domain. The time step is chosen as $\Delta t = 2 \times 10^{-11}$ s. The proposed method takes 13.63 MB to store $\mathbf{S}_e$ and $\mathbf{S}_h$, and $3.6 \times 10^{-3}$ s to finish the simulation
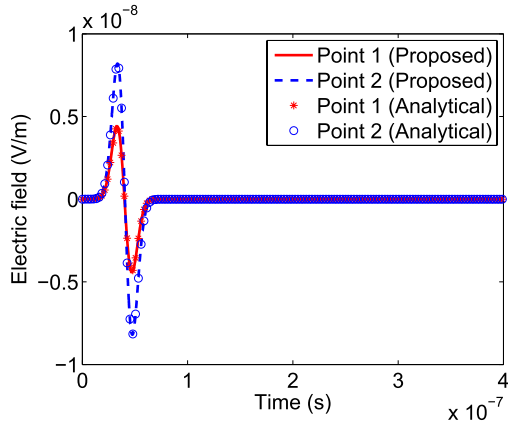
Fig. 10.   Late-time simulation of a rectangular box with a hole.



Fig. 11.   Simulation of a spherical shell discretized into tetrahedral elements. (a) Electric fields obtained from the proposed method as compared with the analytical results. (b) Entire solution error versus time for **E**.
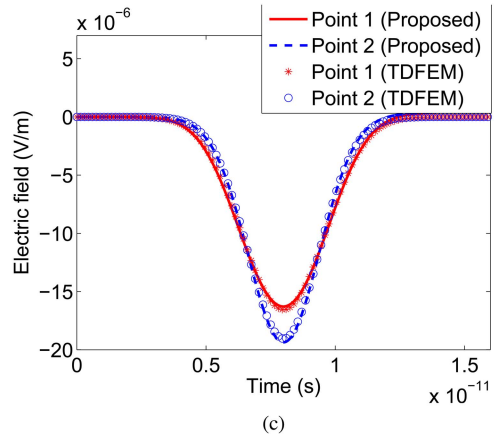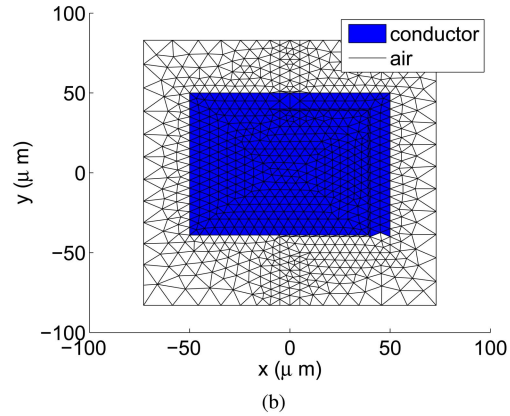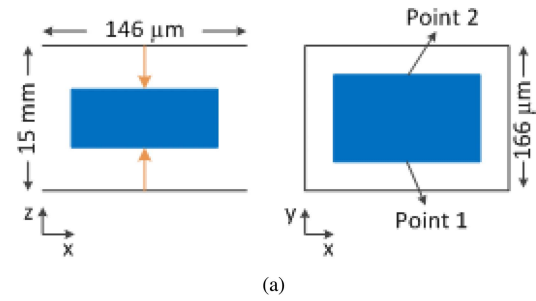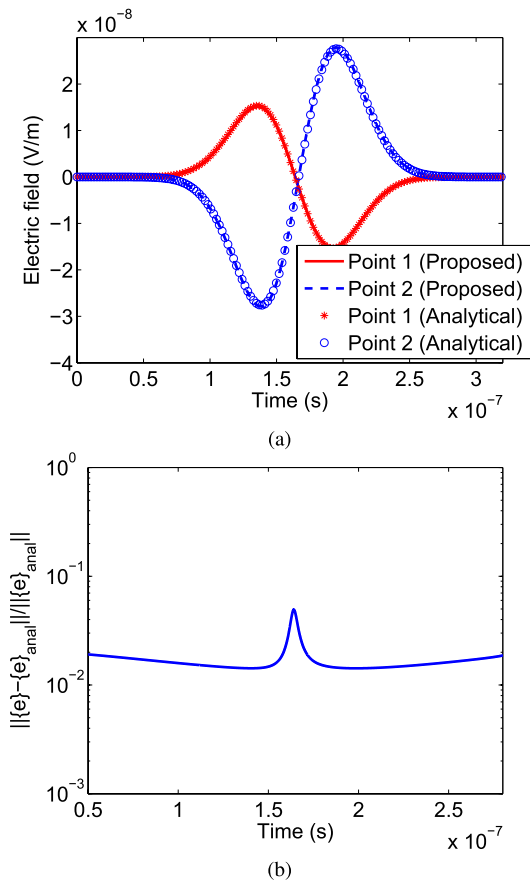


Fig. 12.   Simulation of a lossy and inhomogeneous example discretized into triangular prism elements. (a) Illustration of the structure. (b) Top view of the mesh. (c) Electric fields solved from the proposed method as compared with the TDFEM results.

at one time step. In Fig. 11(a), we plot two electric field unknowns randomly selected from the entire $\{e\}$ vector, whose indices are 1 and 11064. In Fig. 11(b), we plot the entire solution error shown in (41) with respect to time. Excellent agreement with analytical data can be observed from Fig. 11(a) and (b).

### E. Lossy and Inhomogeneous Example Discretized Into Triangular Prism Elements

Previous examples are all in free space. In this example, we simulate a structure with lossy conductors and inhomogeneous

materials shown in Fig. 12(a). The structure is discretized into three layers of triangular prism elements. The thickness of each layer is 5 mm. The top view of the mesh is shown in Fig. 12(b). The aspect ratio of the triangular mesh on the $xy$ plane is 15.18. The discretization results in 12 574 triangular prism elements and 5022 edges. A square conductor is located at the center of the second layer, which is shown in blue in Fig. 12(b). The metal conductivity is $5 \times 10^7$ S/m. The second layer is filled by a material of dielectric constant 4. The rest of the two layers have dielectric constant 1. The top and bottom boundaries are truncated by perfect electric conducting (PEC) boundary condition, while perfect magnetic conductor (PMC) boundary condition is imposed on the other four sides. A current source with a Gaussian's derivative pulse
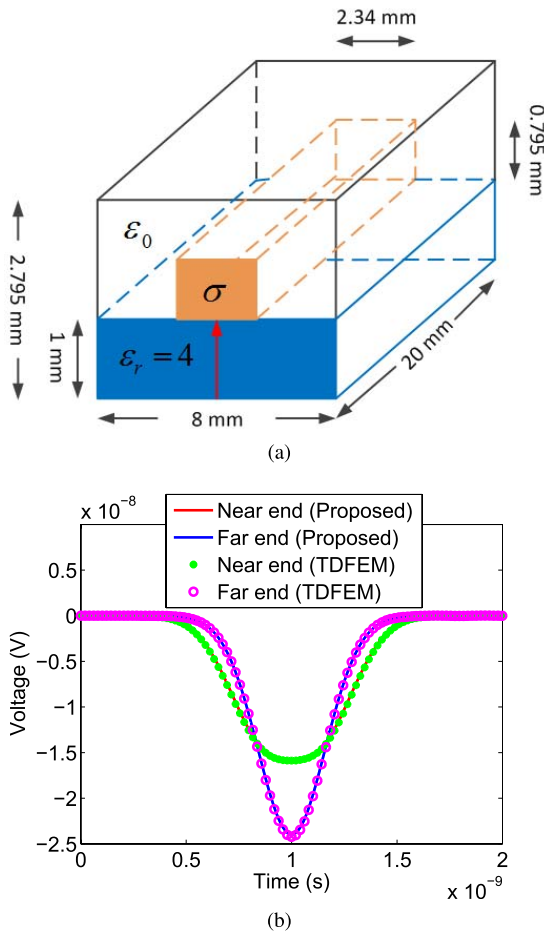
Fig. 13.  (a) Illustration of the microstrip line. (b) Voltages simulated from the proposed method compared with the TDFEM results.
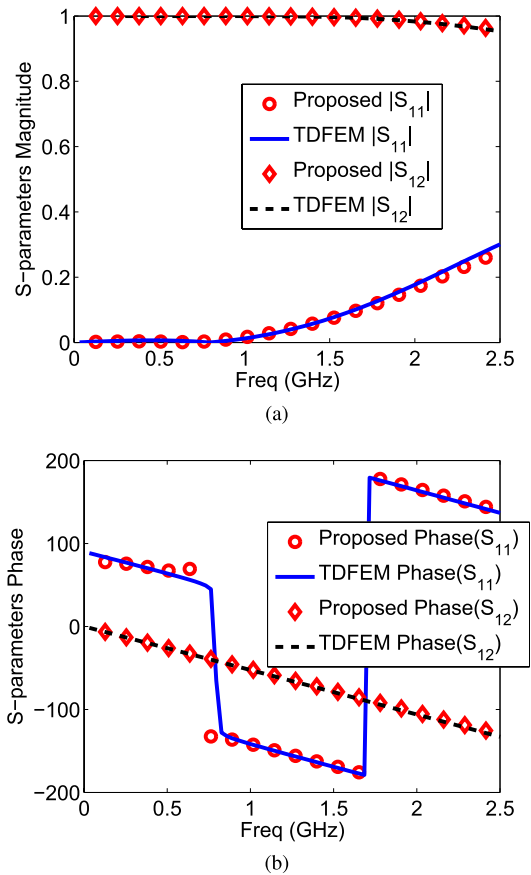


Fig. 14.  Simulation of a lossy and inhomogeneous microstrip line discretized into tetrahedral elements. (a) S-parameter magnitude. (b) S-parameter phase (degrees).

is launched having $\tau = 2 \times 10^{-12}$ s. $\Delta t = 5 \times 10^{-16}$ s is chosen, since the smallest size has a micrometer dimension. The proposed method takes 0.12 GB to store sparse $\mathbf{S}_e$ and $\mathbf{S}_h$, and 0.10 s to finish the simulation at one time step. To examine the accuracy of the proposed method, we simulate the same example by using the TDFEM as the reference. Fig. 12(c) compares the simulated electric fields at two observation points located at the front and back end of the square conductor with those simulated by TDFEM. Excellent agreement is observed.

### F. Lossy and Inhomogeneous Microstrip Line Discretized Into Tetrahedral Elements

In this example, we simulate a 20-mm-long inhomogeneous and lossy microstrip line discretized into tetrahedral elements. The structure details can be found in Fig. 13(a). The aspect ratio of the tetrahedral mesh is 8.78. The substrate has a material of $\epsilon_r = 4$. The conductivity of the metal strip is $5.8 \times 10^7$ S/m. The discretization results in 35 283 edges and 28 365 tetrahedrons. A current source is imposed at the near end with $j = 2(t - t_0) \exp(-(t - t_0/\tau)^2)$ and $\tau = 2.5 \times 10^{-10}$ s. The bottom plane is terminated with PEC, while PMC is applied to other boundaries. The time step used is $6 \times 10^{-14}$ s. The proposed method takes only 0.22 GB to store sparse $\mathbf{S}_e$ and $\mathbf{S}_h$, and 0.10 s to finish the simulation

at one time step. The voltage between the microstrip and the ground plane at the near end ($z = 0$) and far end ($z = 20$ mm) is extracted, and compared with the reference TDFEM solution in Fig. 13(b). It is evident that the results obtained from the proposed method agree very well with the reference results. In Fig. 14, we plot the S-parameters extracted from the time-domain waveforms of the proposed method in comparison with those generated from TDFEM. Excellent agreement is observed in the entire frequency band simulated.

### G. CPU Time and Memory Comparison

In this section, we simulate a large example to compare the performance of the proposed matrix-free method against the TDFEM which is equally capable of handling unstructured meshes, but not free of matrix solutions. This example is a circular cylinder of radius 1 m discretized into 25 layers of triangular prism elements. The incident field is a plane wave having a Gaussian's derivative pulse with $\tau = 10^{-8}$ s. An analytical absorbing boundary condition is imposed at the outermost boundary. The discretization results in 3 718 900 $\mathbf{E}$ unknowns using the zeroth-order TDFEM. A similar number of unknowns, 3 741 700 $\mathbf{E}$ unknowns, is generated in the proposed method for a fair comparison. Since TDFEM requires solving a mass matrix, we perform the LU factorization of the sparse mass matrix once before time marching, and use backward/forward substitution to obtain the solution at each time step. The TDFEM takes 2267.71 s and more than 72-GB

memory to finish the factorization. This large memory cost is due to the fact that although the matrix being factorized is sparse, its **L** and **U** factors are generally dense. During time marching, the TDFEM costs 9.22 s at each time step. In contrast, since the proposed method is matrix-free, it does not need any memory as well as CPU time to factorize and solve the matrix. It takes only 5.2-GB memory to store the sparse $\mathbf{S}_e$ and $\mathbf{S}_h$, and 2.7 s for performing the time marching for one time step. Obviously, the proposed method significantly outperforms TDFEM in terms of computational efficiency. As for accuracy, the entire solution error across the whole time window is $<0.01\%$ for TDFEM and 0.05% for the proposed method, as compared with the analytical result. Therefore, the proposed method can achieve a similar level of good accuracy as TDFEM. The difference in accuracy can be attributed to the difference in space as well as time discretizations of the two methods.
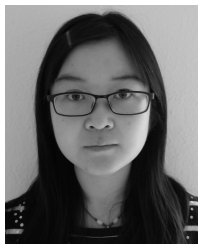
## IV. CONCLUSION

In this paper, a new matrix-free time-domain method with a modified-basis formulation is developed for solving Maxwell's equations in general 3-D unstructured meshes. The method is naturally free of matrix solutions. No mass lumping is required, as the mass matrix is diagonal in nature by the proposed algorithm of discretizing Maxwell's equations. The method handles arbitrary unstructured meshes with the same ease as an FEM. It overcomes the absolute instability of an explicit method when an unsymmetrical operator having complex-valued and even negative eigenvalues is involved. Both stability and accuracy are theoretically guaranteed, and the tangential continuity of the fields is enforced at the material interfaces. It does not require dual mesh, projection, and interpolation. Unlike our previous 3-D formulation, a set of modified vector basis functions are developed to directly connect the discretized Ampere's law with the discretized Faraday's law without any need for unknown transformation. Extensive numerical experiments on unstructured tetrahedral and triangular prism meshes, involving inhomogeneous, lossless, as well as lossy materials, have validated the accuracy, generality, and matrix-free property of the proposed method.

It is also worth mentioning that the proposed method can be flexibly extended to achieve any desired higher order accuracy by expanding one field unknown using arbitrary-order vector bases, and sampling the other field unknown in the loop orthogonal to the first field unknown in a higher order way. The modified higher order vector bases developed in this paper can also be used in any other method that employs higher order bases. With these new bases, the relationship is explicitly known between unknown fields and unknown coefficients of vector bases. The approach developed here and in [16] for stably simulating an unsymmetrical curl–curl operator can also be leveraged by the existing nonorthogonal FDTD methods for controlling stability.

## REFERENCES

[1] K. Yee, "Numerical solution of initial boundary value problems involving Maxwell's equations in isotropic media," *IEEE Trans. Antennas Propag.*, vol. AP-14, no. 3, pp. 302–307, May 1966.

[2] A. Taflove and S. C. Hagness, *Computational Electrodynamics: The Finite-Difference Time-Domain Method*. Boston, MA, USA: Artech House, 2000.

[3] R. Holland, "Finite-difference solution of Maxwell's equations in generalized nonorthogonal coordinates," *IEEE Trans. Nucl. Sci.*, vol. NS-30, no. 6, pp. 4589–4591, Dec. 1983.

[4] M. Fusco, "FDTD algorithm in curvilinear coordinates [EM scattering]," *IEEE Trans. Antennas Propag.*, vol. 38, no. 1, pp. 76–89, Jan. 1990.

[5] T. G. Jurgens and A. Taflove, "Three-dimensional contour FDTD modeling of scattering from single and multiple bodies," *IEEE Trans. Antennas Propag.*, vol. 41, no. 12, pp. 1703–1708, Dec. 1993.

[6] S. Dey and R. Mittra, "A locally conformal finite-difference time-domain (FDTD) algorithm for modeling three-dimensional perfectly conducting objects," *IEEE Microw. Guided Wave Lett.*, vol. 7, no. 9, pp. 273–275, Sep. 1997.

[7] S. Gedney, F. S. Lansing, and D. L. Rascoe, "Full wave analysis of microwave monolithic circuit devices using a generalized Yee-algorithm based on an unstructured grid," *IEEE Trans. Microw. Theory Techn.*, vol. 44, no. 8, pp. 1393–1400, Aug. 1996.

[8] A. Bossavit and L. Kettunen, "Yee-like schemes on a tetrahedral mesh, with diagonal lumping," *Int. J. Numer. Model.-Electron. Netw. Devices Fields*, vol. 12, nos. 1–2, pp. 129–142, 1999.

[9] C. F. Lee, B. J. McCartin, R. T. Shin, and J. A. Kong, "A triangular-grid finite-difference time-domain method for electromagnetic scattering problems," *J. Electromagn. Waves Appl.*, vol. 8, no. 4, pp. 449–470, 1994.

[10] M. Hano and T. Itoh, "Three-dimensional time-domain method for solving Maxwell's equations based on circumcenters of elements," *IEEE Trans. Magn.*, vol. 32, no. 3, pp. 946–949, May 1996.

[11] S. D. Gedney and J. A. Roden, "Numerical stability of nonorthogonal FDTD methods," *IEEE Trans. Antennas Propag.*, vol. 48, no. 2, pp. 231–239, Feb. 2000.

[12] M. Cinalli and A. Schiavoni, "A stable and consistent generalization of the FDTD technique to nonorthogonal unstructured grids," *IEEE Trans. Antennas Propag.*, vol. 54, no. 5, pp. 1503–1512, May 2006.

[13] H.-X. Zheng and K. W. Leung, "A nonorthogonal ADI-FDTD algorithm for solving two dimensional scattering problems," *IEEE Trans. Antenna Propag.*, vol. 57, no. 12, pp. 3891–3902, Dec. 2009.

[14] M. M. Rana and A. S. Mohan, "Nonorthogonal LOD-FDTD method for EM scattering from two-dimensional structures," *IEEE Trans. Electromagn. Compat.*, vol. 55, no. 4, pp. 764–772, Aug. 2013.

[15] R. T. Lee, J. G. Maloney, B. N. Baker, and D. W. Landgren, "FDTD in curvilinear coordinates using a rectangular FDTD formulation," in *Proc. IEEE Int. Symp. Antennas Propag.*, Jul. 2011, pp. 2326–2329.

[16] J. Yan and D. Jiao, "Accurate and stable matrix-free time-domain method in 3-D unstructured meshes for general electromagnetic analysis," *IEEE Trans. Microw. Theory Techn.*, vol. 63, no. 12, pp. 4201–4214, Dec. 2015.

[17] D. Jiao and J. Jin, "Finite element analysis in the time domain," in *The Finite Element Method in Electromagnetics*. New York, NY, USA: Wiley, 2002, pp. 529–584.

[18] D. A. White, "Orthogonal vector basis functions for time domain finite element solution of the vector wave equation [EM field analysis]," *IEEE Trans. Magn.*, vol. 35, no. 3, pp. 1458–1461, May 1999.

[19] D. Jiao and J.-M. Jin, "Three-dimensional orthogonal vector basis functions for time-domain finite element solution of vector wave equations," *IEEE Trans. Antennas Propag.*, vol. 51, no. 1, pp. 59–66, Jan. 2003.

[20] S. D. Gedney et al., "The discontinuous Galerkin finite element time domain method (DGFETD)," in *Proc. IEEE Int. Symp. Antennas Propag.*, Aug. 2008, pp. 1–4.

[21] S. D. Gedney, J. C. Young, T. C. Kramer, and J. A. Roden, "A discontinuous Galerkin finite element time-domain method modeling of dispersive media," *IEEE Trans. Antennas Propag.*, vol. 60, no. 4, pp. 1969–1977, Apr. 2012.

[22] J. Yan and D. Jiao, "Formulations of an accurate and stable matrix-free time-domain method in 2-D unstructured meshes," in *Proc. IEEE MTT-S Int. Conf. Numer. Electromagn. Multiphys. Modeling Optim. (NEMO)*, Aug. 2015, pp. 1–3.

[23] J. Yan and D. Jiao, "Accurate matrix-free time-domain method in unstructured meshes," in *IEEE MTT-S Int. Microw. Symp. Dig.*, May 2015, pp. 1–4.

[24] J. Yan and D. Jiao, "Accurate matrix-free time-domain method with traditional vector bases in unstructured meshes," in *Proc. IEEE Int. Symp. Antennas Propag.*, Jul. 2015, pp. 1–2.
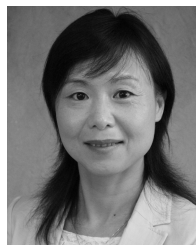
[25] J. Yan and D. Jiao, "Accurate and stable matrix-free time-domain method independent of element shape for general electromagnetic analysis," in *Proc. Int. Conf. Electromagn. Adv. Appl. (ICEAA)*, Sep. 2015, pp. 1–4.

[26] J. Yan and D. Jiao, "Accurate matrix-free time-domain method in three-dimensional unstructured meshes," in *Proc. IEEE Int. Symp. Antennas Propag.*, Jul. 2015, pp. 1830–1831.

[27] R. D. Graglia, D. R. Wilton, and A. F. Peterson, "Higher order interpolatory vector bases for computational electromagnetics," *IEEE Trans. Antennas Propag.*, vol. 45, no. 3, pp. 329–342, Mar. 1997.

**Dan Jiao** (M'02–SM'06–F'16) received the Ph.D. degree in electrical engineering from the University of Illinois at Urbana–Champaign, Champaign, IL, USA, in 2001.

She was with the Technology Computer-Aided Design (CAD) Division, Intel Corporation, Santa Clara, CA, USA, until 2005, as a Senior CAD Engineer, Staff Engineer, and Senior Staff Engineer. In 2005, she joined the School of Electrical and Computer Engineering, Purdue University, West Lafayette, IN, USA, as an Assistant Professor, where she is currently a Professor. She has authored 3 book chapters and over 230 papers in refereed journals and international conferences. Her current research interests include computational electromagnetics, high-frequency digital, analog, mixed-signal, and RF integrated circuit design and analysis, high-performance VLSI CAD, modeling of microscale and nanoscale circuits, applied electromagnetics, fast and high-capacity numerical methods, fast time-domain analysis, scattering and antenna analysis, RF, microwave, millimeter-wave circuits, wireless communication, and bioelectromagnetics.

Dr. Jiao was the recipient of the 2013 S. A. Schelkunoff Prize Paper Award of the IEEE Antennas and Propagation Society, which recognizes the best paper published in the IEEE TRANSACTIONS ON ANTENNAS AND PROPAGATION during the previous year. She was a recipient of the 2010 Ruth and Joel Spira Outstanding Teaching Award, the 2008 National Science Foundation CAREER Award, the 2006 Jack and Cathie Kozik Faculty Start Up Award (which recognizes an Outstanding New Faculty Member of the School of Electrical and Computer Engineering, Purdue University), a 2006 Office of Naval Research Award under the Young Investigator Program, the 2004 Best Paper Award at the Intel Corporation's Annual Corporate-Wide Technology Conference (Design and Test Technology Conference) for her work on generic broadband model of high-speed circuits, the 2003 Intel Corporations Logic Technology Development (LTD) Divisional Achievement Award, the Intel Corporation's Technology CAD Divisional Achievement Award, the 2002 Intel Corporation's Components Research the Intel Hero Award (Intel-wide she was the tenth recipient), the Intel Corporations LTD Team Quality Award, and the 2000 Raj Mittra Outstanding Research Award of the University of Illinois at Urbana–Champaign. She has served as the Reviewer for many IEEE journals and conferences. She is an Associate Editor of the IEEE TRANSACTIONS ON COMPONENTS, PACKAGING, AND MANUFACTURING TECHNOLOGY. She was among the 21 women faculty members selected across the country as a 2014–2015 Fellow of the Executive Leadership in Academic Technology and Engineering at Drexel University, a national leadership program for women in the academic STEM fields. She has been named a University Faculty Scholar by Purdue University since 2013. She was among 85 engineers selected throughout the nation for the National Academy of Engineering's 2011 U.S. Frontiers of Engineering Symposium.

**Jin Yan** (GSM'13) received the B.S. degree in electronic engineering and information science from the University of Science and Technology of China, Hefei, China, in 2012. She is currently pursuing the Ph.D. degree in electrical engineering at Purdue University, West Lafayette, IN, USA.

She is with the On-Chip Electromagnetics Group, Purdue University. Her current research interests include computational electromagnetics, high-performance VLSI CAD, and fast and high-capacity numerical methods.

Mrs. Yan was a recipient of an Honorable Mention Award of the IEEE International Symposium on Antennas and Propagation in 2015 and a Best Student Paper Award Finalist from the IEEE MTT-S International Microwave Symposium in 2016.